Advances in imaging shallow fault zone deformation with differential lidar: a VISES Collaboration (SCEC award #14101)

Edwin Nissen (Colorado School of Mines), J Ramon Arrowsmith, Srikanth Saripalli (Arizona State University), Mike Oskin (UC Davis)

1. Summary of major research findings

In this project, we have used two recent earthquakes in Japan to demonstrate the rich potential, as well as some of the challenges, of differencing repeat airborne light detection and ranging (lidar) topographic data to measure coseismic fault zone deformation. We focus on densely-vegetated sections of the 14 June 2008 Iwate-Miyagi (M_w 6.9) and 11 April 2011 Fukushima-Hamadori (M_w 7.1) earthquake ruptures, each covered by 2 m-resolution pre-event and 1 m-resolution post-event bare Earth digital terrain models (DTMs) obtained from commercial lidar providers.

3-dimensional displacements and rotations were extracted from these datasets using an adaptation of the Iterative Closest Point (ICP) algorithm. These displacements remain coherent close to surface fault breaks, as well as within dense forest, despite intervals of ~2 years (Iwate-Miyagi) and ~4 years (Fukushima-Hamadori) encompassed by the lidar scenes. Differential lidar analysis is thus complimentary to Interferometric Synthetic Aperture Radar (InSAR) and sub-pixel correlation techniques which often break down under conditions of long time intervals, dense vegetation, or steep displacement gradients. Although the ICP displacements are much noisier than overlapping InSAR line-of-sight displacements, they still provide powerful constraints on near-surface fault slip. In the Fukushima-Hamadori case, near-fault displacements and rotations are consistent with decreased primary fault slip at very shallow depths of a few 10s of meters, possibly accounting for the large, along-strike heterogeneity in fault slip observed in the field.

Work on these datasets is continuing under a no-cost extension to the project, but our preliminary findings were published in *Earth and Planetary Science Letters* in late 2014 (Nissen *et al.,* 2014). Much of this report is taken directly from that publication, although this report focuses exclusively on the 2008 Iwate-Miyagi earthquake for reasons of space limitation. We refer the reader to the paper for more details, and for a description of our work on the 2011 Fukushima-Hamadori event.

Work is underway on differencing the complete lidar coverages for both earthquakes (rather than the smaller scenes presented in our paper), using the raw points clouds rather than the gridded, bare Earth DTMs. We envisage a follow-up paper describing these efforts in late 2015. We have also been active in presenting and disseminating this work widely, at meetings and workshops including SCEC, UJNR (Sendai, Japan), GSA, AGU, and RAS (London, UK).

2. Technical report

2.1 Project objectives

Over the past two decades, Interferometric Synthetic Aperture Radar (InSAR) and optical or SAR amplitude pixel matching techniques have enabled coseismic surface deformation to be mapped over wide regions and at dense spatial resolutions (e.g., Masonnet *et al.,* 1993; Michel *et al.,* 1999). These data are crucial for identifying the causative faulting and interpreting the long-term record of earthquakes recorded in topography. By resolving surface displacements into patterns of slip at depth, the transfer of stresses onto neighboring faults can also be estimated (e.g., Fialko, 2004). However, these methods are hampered by certain restrictions. (1) They measure only particular components of the 3-dimensional (3-D) deformation field. (2) C-band InSAR and sub-pixel correlation techniques often break down in regions with forest or agricultural cover. (3) While InSAR is powerful at detecting the far-field deformation of continental earthquakes caused by slip at depth, steep phase gradients and intense ground shaking often lead to loss of coherence within and along the fault zone itself, limiting our constraints upon the shallow slip distribution.

The differencing of pre- and post-earthquake topography offers rich potential for addressing these limitations. Airborne Light Detection and Ranging (lidar), also known as airborne laser swath mapping (ALSM), uses a laser ranging device, together with information on the position and orientation of the aircraft platform, to determine the *x*, *y* and *z* coordinates of an uneven distribution of ground targets (a "point cloud") to a precision of a few centimetres (e.g., Carter *et al.,* 2007). Modern lidar surveys can map wide regions at densities of several points/m^2 or higher and can also record multiple returns from a single laser pulse, such as from canopy layers and the underlying ground surface. This capability allows vegetation to be removed from lidar point clouds, and has been used to reveal previously unidentified fault scarps in densely forested regions (e.g., Haugerud *et al.,* 2003).

As the point spacing in modern lidar datasets is finer than the scale of slip in large earthquakes, differencing of 'before' and 'after' fault zone topography should reveal 3 dimensional (3-D) coseismic surface displacements without loss of coherence in vegetated areas or rupture zones. An explosion of lidar surveying in the past decade provides a topographic baseline for future differencing opportunities along many active faults, particularly in the western US (e.g., Bevis *et al.,* 2005; Prentice *et al.,* 2009). However, demonstration of this emerging new application for airborne lidar has so far been restricted by a lack of high quality paired datasets on which to test them. The 2010 El Mayor-Cucapah earthquake rupture in northern Mexico is the only earthquake with complete pre- and post- lidar coverage, but 3-D analysis of the deformation field is made difficult by the unusually sparse density (~0.013 points/m^2) of the pre-event dataset (Oskin *et al.,* 2012; Glennie *et al.,* 2014). Experiments on southern California lidar datasets deformed with simulated earthquakes of known displacements reveal what should be possible with higher density point clouds (Borsa & Minster, 2012; Nissen *et al.,* 2012). In addition, all of these studies focus on semi-arid landscapes where vegetation cover is not a serious issue for lidar differencing, as it will be in many future cases.

Here, we exploit two, newly-available, paired lidar datasets to map 3-D fault zone deformation along portions of two recent earthquake ruptures in Japan (Figure 1). Both events occurred in regions with dense forested cover, allowing us to explore lidar differencing in more challenging conditions than was previously possible. The Japanese pre-event data are much higher-resolution than those at El Mayor-Cucapah, so these new examples also provide a truer test of the future potential of lidar differencing.

2.2 Introduction to the 2008 Iwate-Miyagi earthquake (M_w 6.9)

This event struck north-eastern Honshu on 14 June 2008, in a mountainous region along the border of the Iwate and Miyagi prefectures, ~400 km north of Tokyo (Figure 1a). Ascribed a local magnitude (M_{jma}) of 7.2 by the Japanese Meteorological Agency (JMA) and a moment magnitude (M_w) of 6.9 by the Global Centroid Moment Tensor (GCMT) catalog, this was the largest inland earthquake in Japan since the devastating 1995 Kobe event (M_{jma} 7.3, M_w 6.9), and it led to 23 people dying or going missing, ~500 injuries, and heavy damage to more than 100 buildings. The earthquake also triggered more than 4,100 mapped landslides and debris flows which contributed greatly to the loss of life and property in the area (Yagi *et al.,* 2009).

Source models based on near-field high rate GPS and strong motion data show that the earthquake involved predominantly reverse slip on a ~40 km-long, NNE-striking and WNW-dipping fault (Ohta *et al.,* 2008; Yokota *et al.,* 2009; Suzuki *et al.,* 2010; Lucca *et al.,* 2012). InSAR models for the earthquake are in general agreement, but also incorporate slip on a conjugate ESE-dipping fault in the central part of the fault zone (Takada *et al.,* 2009; Abe *et al.,* 2013). According to these models, peak slip was 1 – 3 m in the northern part of the fault zone and 3.5 – 6.5 m in the southern part and occurred at a depth of 2 – 5 km. The causative fault, which had not been identified prior to the earthquake, broke along the eastern flank of the Ou Mountains (Figure 1b), a range that is mainly composed of Miocene–Quaternary volcanic and sedimentary rocks (Toda *et al.,* 2010). InSAR measurements were hindered by poor coherence in much of the hanging-wall as well as along parts of the surface rupture, including the entire area of double LiDAR coverage (Figure 1b). Field observations were also hampered by steep, forested terrain in much of the fault zone and only a few, isolated field measurements of surface slip were made (Matsu'ura & Kase, 2010; Toda *et al.,* 2010). Vertical fault offsets are mostly <0.5 m, despite the inference from InSAR modelling of several meters of reverse slip along the fault plane at 2 – 5 km depth (Takada *et al.,* 2009; Abe *et al.,* 2013). An exception to this general pattern was observed in the southern part of the fault zone, where Toda *et al.* (2010) used terrestrial LiDAR measurements to document right-lateral offsets of up to 7 m and vertical offsets of up to 4 m along a ~1 km-long, E-W-striking fault scarp. This section of surface rupture lies within the area of repeat LiDAR coverage focused on in this paper.

In September 2006 the commercial surveying company Kosukai Kogyo Co., Ltd. (http://www.kk-grp.jp/) acquired LiDAR data over several watersheds in the epicentral region of the future earthquake, primarily for the purpose of land management. These data were collected from an aeroplane platform, which flew at an average height of 2,600 m above ground level (AGL) and carried a 32 kHz Leica Geosystem ALS40 scanner. This survey generated ground return densities averaging ~0.25 points/m^2. After the earthquake struck, another commercial LiDAR provider, Aero Asahi Corporation (http://www.aeroasahi.co.jp/), surveyed parts of the rupture zone during several flights in June, July, August and September 2008.

Deploying a 70 kHz Optech ALTM3100 scanner from a helicopter platform at ~1000 m AGL, they were able to generate average point densities of ~4 points/m^2.

We identified a small (1700 m × 900 m) region within the southern part of the fault zone that was mapped in both surveys. We obtained pre- and post-event, gridded, bare earth digital terrain models (DTMs) – shown in Figure 2a and 2b – although we were not provided information about the steps taken rasterize the raw points clouds and remove vegetation. The pre- and post-earthquake DTMs have resolutions of 2 m and 1 m, respectively, and both are registered in Japan Plane Rectangular Coordinate System X (in meters). Most of the area covered by the LiDAR scenes is densely forested (Figure 2c). Within the scene boundaries, there is no clear evidence for the presence of an active fault in the pre-event DTM. The post-event DTM includes a ~1 km-long section of fault scarp, shown at greater magnification in Figure 2d and photographed in Figure 2e. The eastern portion of the scarp faces south (N-side up) and the western portion of which faces north (S-side up). This is the same section of scarp described in detail by Toda et al. (2010). Two major, deep-seated landslides triggered by the earthquake also lie within or partly within the focus area of this study. Part of the Aratozawa landslide – the largest of those triggered by the earthquake with a volume of ~70 million cubic meters (Yagi *et al.,* 2009) – is covered by the SW corner of the scene (Figure 2b, 2c), while the Sanhazama landslide lies in the scene center (Figure 2b, 2c, 2f).

2.3 Methodology

For an initial analysis we subtract the pre-earthquake DTM from the post-earthquake DTM (e.g., Oskin *et al.,* 2012). Although this simple differencing leads to aliasing of tectonic horizontal deformation, it nevertheless clearly reveals large negative and positive elevation changes in the central parts of the scene related to the scarp and toe of the Sanhazama landslide, respectively (Figure 3a). The landslide has in turn blocked and dammed the E-flowing Sanhazama River, which consequently displays positive elevation changes of a few meters along its upper course. The scarp of the Aratozawa landslide in the SW corner of the scene is also characterized by strong negative elevation changes. Linking the two landslide scarps, the ~1 km-long fault scarp mapped by Toda *et al.* (2010) is also marked by a faint discontinuity in elevation difference values. However, the simple elevation differencing does not measure horizontal motions and it is therefore difficult to discern additional information about coseismic displacements from this map. Conversely, Mukoyama (2012) applied particle image velocimetry (PIV) to LiDAR slope maps to obtain horizontal displacements across this area (using a different post-event dataset to the one we use), but this method does not account for vertical changes.

To construct the 3-D surface deformation field we used Nissen *et al.*'s (2012) implementation of the Iterative Closest Point (ICP) algorithm (Besl & McKay, 1992; Chen & Medioni, 1992). It computes surface displacements and rotations by iteratively minimizing closest point distances between local square subsets ("cells") of the pre-event ("source") and post-event ("target") data (Figure 4). The resulting (cumulative) rigid-body transformation represents the local displacement and rotation that most closely aligns the pre-event cell topography to the post-event equivalent. The choice of cell dimension must balance the desire for finer resolution against the requirement that each cell contain enough topographic heterogeneity for an accurate alignment to be achievable (pairs of cells that contain planar

arrays of points can, of course, be aligned in any number of ways and so in very flat areas or on completely planar slopes ICP results may be meaningless). In addition, larger cell sizes risk there being significant internal strain arising from the displacement field, which would prevent alignment through the ICP rigid body transformation. However, Nissen *et al.* (2012) showed that realistic elastic deformation gradients have negligible effects on computed ICP displacements for the cell sizes considered in this study.

Taking these factors into consideration and after experimentation, we used a cell size of 50 x 50 m. The target cells also included an additional 10 m-wide overlapping border in order to fully capture the coseismic displacement and thus ensure that topographic features in each pre-event cell are contained within the post-event cell. Although the method is easily applied to irregularly-spaced point clouds, here we were restricted to using the regularly-spaced nodes of the DTMs. This potentially introduces a bias in computed displacements, because certain alignments of regularly-spaced grids achieve closer horizontal closest point distances than others. For this reason, we chose to use point-to-plane ICP (Chen & Medioni, 1992) which minimizes distances between each source point and the tangential plane at its target point.

Results

The ICP differencing clearly reveals the 3-D coseismic displacement field across the scene (Figure 3b), in stark contrast with the simple elevation differencing (Figure 3a). In this simple implementation of the ICP algorithm, there is no overlap between adjacent "source" cells and the displacement value for each cell is therefore obtained independently from those of its neighbors. This gives us confidence that the smoothly-varying displacements observed across most of the scene are genuine. It also implies that there is no limit to the displacement gradients resolvable between adjacent cells, as long as the internal cell strain is not so large that ICP cannot compute a meaningful rigid-body alignment in the first place (as discussed earlier). In practice this means that ICP yields mostly spurious displacements for cells that contain the fault scarp – these have been removed from Figure 3b – but yields coherent displacements for cells in very close proximity to the surface break including neighbouring ones. This is in stark contrast with conventional InSAR, where line-of-sight displacement gradients of more than one radar half-wavelength (typically a few centimeters) per pixel (typically a few tens of meters) result in incoherent noise. In this example, InSAR imagery is completely decorrelated within the extents of the LiDAR scene (Figure 1b; Midorikawa & Miura, 2008; Takada *et al.,* 2009). This is despite the fact that the two LiDAR datasets encompass a ~2 year interval compared to the ~1 year timespan of the interferogram shown in Figure 1b.

In addition to the DTM cells which contain the fault scarp, those encompassing the two landslides and the dammed river also involve a change in internal cell shape, rendering ICP alignments spurious. Displacements in these cells are consequently eliminated from Figure 3b. These areas are instead best characterized by the elevation difference map in Figure 3a. There remains the potential to use ICP and PIV to detect block surface motions occurring within deep-seated landslides (Teza *et al.,* 2007; Aryal *et al.,* 2012), but the two contained within our scene each involved incoherent collapse of the hillside rendering these methods challenging or even impossible.

Discounting cells containing the fault scarp or which cover the two landslides or the dammed river, the entire scene contains coherent ICP displacements (Figure 3b). The NW side of the fault generally translates eastwards relative to the SE side, consistent with published focal mechanisms and fault models (e.g. Takada *et al.,* 2009). Displacements in cells on either side of the E-W trending fault scarp therefore indicate significant right-lateral slip as well as some vertical slip, switching from N-side up to S-side up along the westernmost part of the scarp, in agreement with field observations (Toda *et al.,* 2010). In the region between the scarp and the dammed Sanhazama river, material rotates anticlockwise around a vertical axis such that adjacent to the landslide scar, surface displacements are to the NE. However, N of the dammed river, displacements are uniformly towards the SE. The resultant discontinuity in displacements across the Sanhazama river may reflect (1) shallow faulting along the trend of the river channel or (2) NE-directed slumping of the southern flank of the Sanhazama valley. Superficially, our horizontal displacement field resembles the one obtained from particle image velocimetry (Mukoyama, 2012).

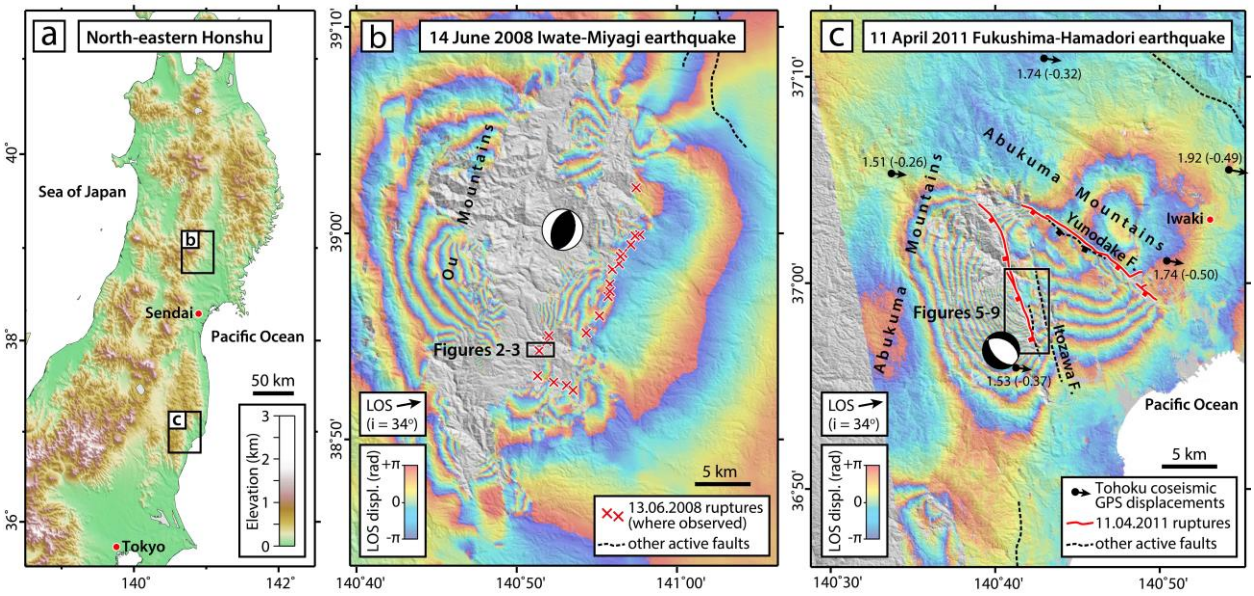

Figure 1. (a) Topographic map of north-eastern Honshu, Japan. **(b)** The epicentral region of the 14 June 2008 Iwate-Miyagi earthquake (Mw 6.9) showing the Global CMT catalog focal mechanism, the locations of mapped surface ruptures from Matsu'ura & Kase (2010) and Toda *et al.* (2010), and a coseismic interferogram constructed from ALOS PALSAR ascending track 402 scenes from 21 June 2007 and 23 June 2008 (using JPL/Caltech ROI_PAC software). *i* is the line-of-sight (LOS) incidence angle (measured from the vertical) and 2 π radians in LOS displacement is equivalent to the radar half-wavelength of 11.8 cm (with positive increasing values indicating motion away from the satellite). **(c)** The epicentral region of the 11 April 2011 Fukushima-Hamadori earthquake (Mw 7.1) with mapped surface ruptures from Mizoguchi *et al.* (2012) and Toda & Tsutsumi (2013), the GCMT focal mechanism, and a coseismic interferogram constructed from ALOS PALSAR ascending track 304 scenes from 3 March and 18 April 2011. The fringe pattern near the SW corner of the figure results from an earlier Mw 5.8 (Mj 6.1) earthquake on 19 March 2011 (Kobayashi *et al.,* 2012). We also plot coseismic GPS displacements for the Tohoku earthquake from Ozawa *et al.* (2011); numbers refer to lateral (and vertical) displacements in meters. Other active faults are from Nakata & Imaizumi (2002).

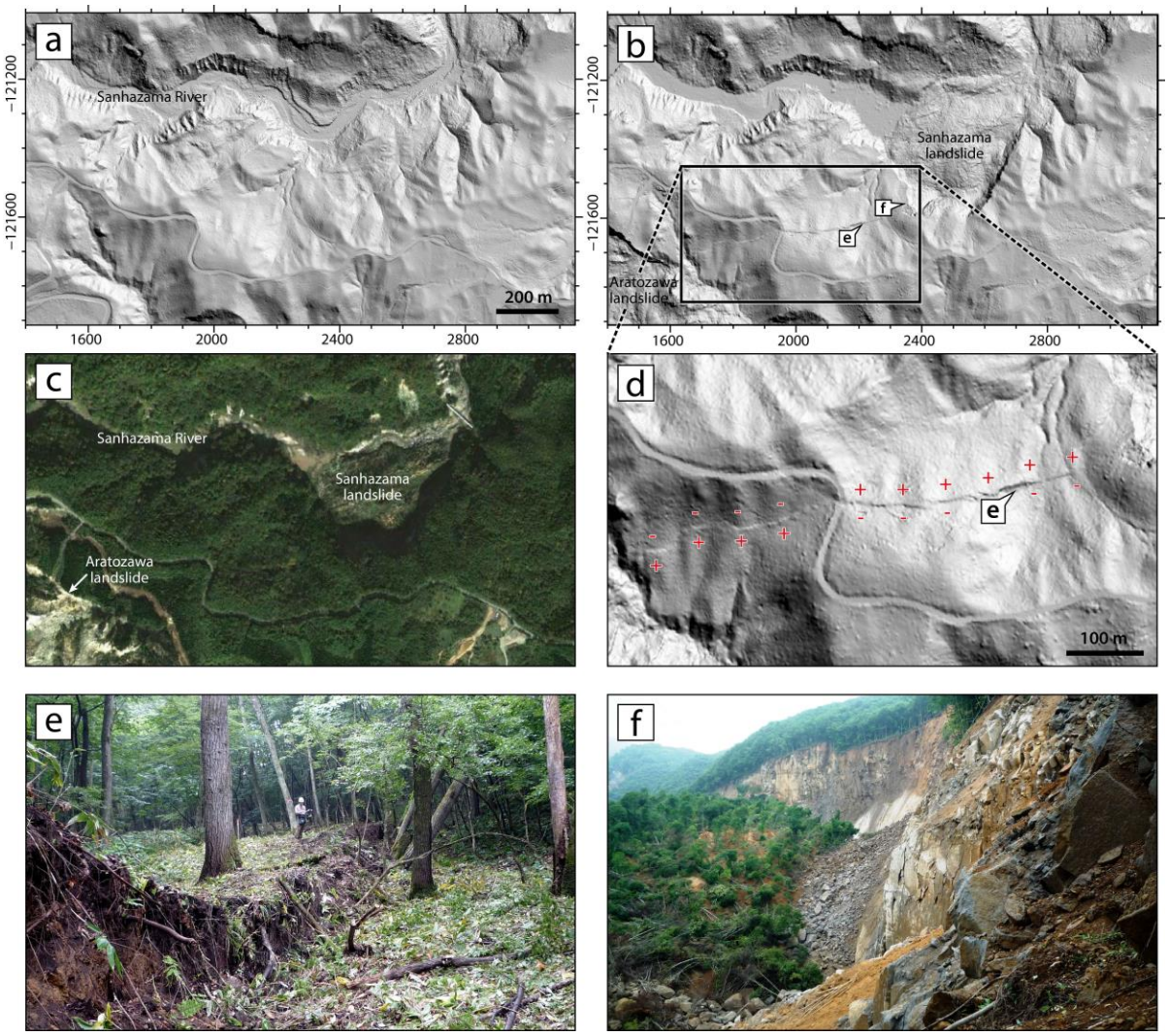

Figure 2. (a) Pre- and **(b)** post-earthquake airborne LiDAR DTMs spanning the 2008 Mw 6.9 Iwate-Miyagi earthquake, artificially illuminated from the NE with x and y coordinates in meters (Japan Plane Rectangular Coordinate System X). **(c)** Post-earthquake Google Earth image of the same scene captured on 15 October 2009. **(d)** Fault scarp in (b) shown at greater magnification. The earthquake scarp is marked in by red pluses on the locally-upthrown side and minuses on the downthrown side. (e) Photograph of surface rupture, facing approximately ENE with geologist for scale. Photograph location shown in (b) and (d). (f) Photograph of the landslide scarp at the head of the Sanhazama landslide, facing approximately E. Photograph location shown in (b). Note the dense forest canopy in photographs and Google Earth image.

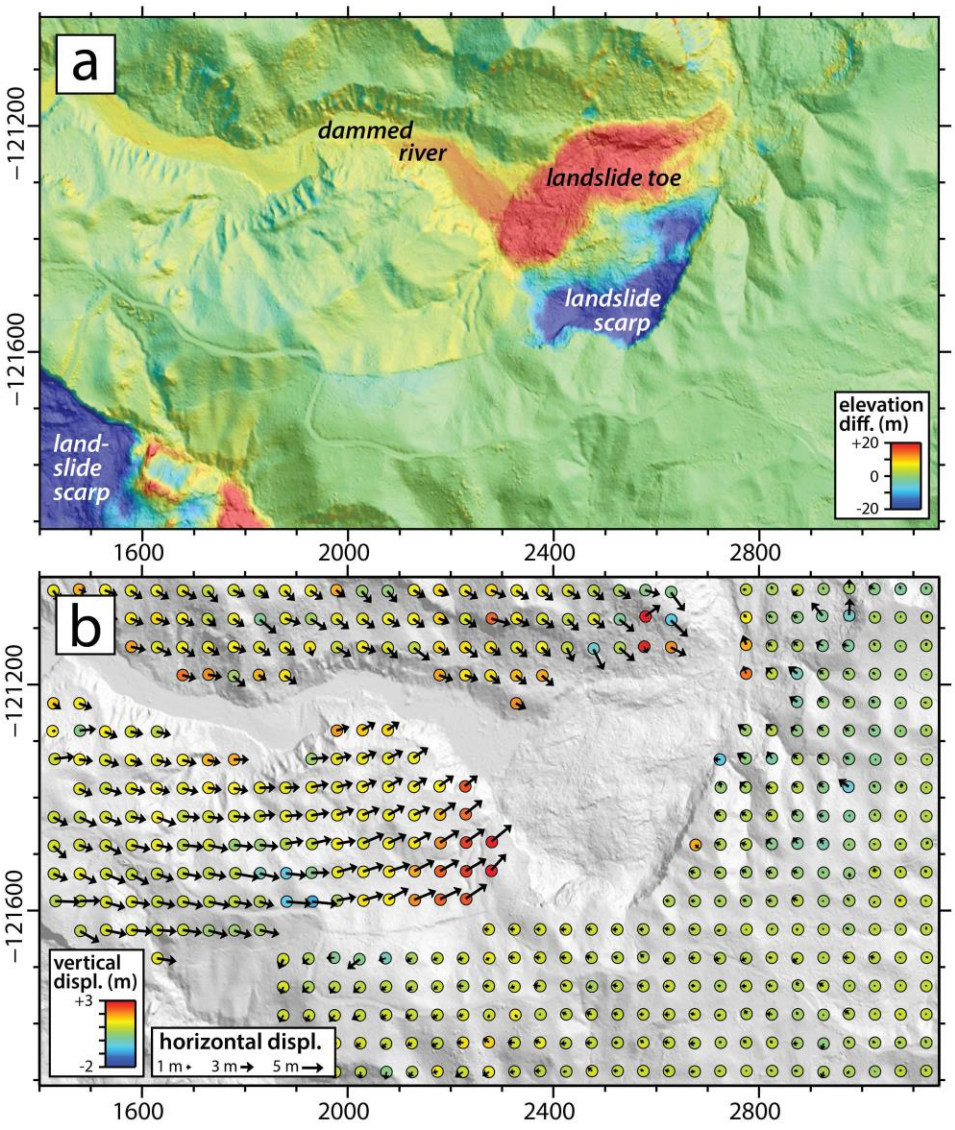

Figure 3. (a) Elevation change for the 2008 M_w 6.9 Iwate-Miyagi earthquake determined by subtracting pre- DTM from post- DTM. **(b)** ICP differencing results: arrows are horizontal displacements and colored circles are vertical displacements. The entire extent of this map is incoherent in InSAR imagery (Figure 1b).

3. Intellectual merit

The 14 June 2008 Iwate-Miyagi (M_w 6.9) and 11 April 2011 Fukushima-Hamadori (M_w 7.1) earthquake ruptures are amongst the first partial earthquake ruptures captured with differential lidar. To our knowledge the only other examples are the 4 April 2010 El Mayor-Cucapah (Mexico) earthquake (Oskin *et al.,* 2012; Glennie *et al.,* 2014), the 4 September 2010 Darfield and 22 February 2011 Christchurch (New Zealand) earthquakes (Duffy *et al.,* 2013), and most recently the 24 August 2014 South Napa (California) earthquake. In areas that contain wide coverage of research-grade lidar such as Southern California, differential lidar analyses of earthquakes will soon become routine. It is therefore important to exploit these early case studies in order to hone our techniques for differencing lidar datasets, and to showcase some of the scientific merit in doing so. In the Japanese examples, we demonstrate how lidar-derived displacements retain coherence in the interior fault zone, where InSAR usually decorrelates, highlighting the utility of these new techniques for mapping shallow fault slip.

4. Broader impacts

The project has helped us develop collaborations and share knowledge with Japanese scientists Tadashi Maruyama and Koji Okumura. It motivated a visit by Dr Maruyama to ASU and CSM universities in Spring 2014, and partially funded Prof. Okumura's trip to the SCEC Annual Meeting in September 2014. These followed a visit to Japan in late 2013 by lead investigators Nissen, Arrowsmith and Oskin, who led a SCEC-supported science workshop on high resolution topography at the Earthquake Research Institute, University of Tokyo (details here: http://www.opentopography.org/index.php/resources/VISES_JPN13). Nissen later also traveled to the 2014 UJNR meeting in Sendai, supported by SCEC, where he presented much of this work in front of leading Japanese and USGS earthquake scientists and agency representatives. Such collaborative activities and active engagement with Japanese scientists are central to the success of the VISES program.

5. Bibliography

Abe, T., Furuya, M., Takada, Y., 2013. Nonplanar Fault Source Modeling of the 2008 Mw 6.9 Iwate–Miyagi Inland Earthquake in Northeast Japan. *Bull. Seismol. Soc. Am.* 103(1), 507-518.

Aryal, A., Brooks, B. A., Reid, M. E., Bawden, G. W., Pawlak G. R., 2012. Displacement fields from point cloud data: Application of particle imaging velocimetry to landslide geodesy. *J. Geophys. Res.* 117, F01029.

Besl, P. J., McKay, N. D., 1992. A method for registration of 3-D shapes. *IEEE Transactions on Pattern Analysis and Machine Intelligence* 14(2), 239-256.

Bevis, M., Hudnut, K., Sanchez, R., Toth, C., Grejner-Brzezinska, D., Kendrick, E., Caccamise, D., Raleigh, D., Zhou, H., Shan, S., Shindle, W., Yong, A., Harvey, J., Borsa, A., Ayoub, F., Shrestha, R., Carter, B., Sartori, M., Phillips, D., Coloma, F., 2005. The B4 Project: Scanning the San Andreas and San Jacinto Fault Zones. *AGU Fall Meeting,* Abstract H34-B01.

Borsa, A., Minster, J. B., 2012. Rapid Determination of Near-Fault Earthquake Deformation Using Differential Lidar. *Bull. Seismol. Soc. Am.* 102, 1335-1347.

Carter, W.E., Shrestha, R.L., Slatton, K.C., 2007. Geodetic laser scanning. *Physics Today* 60, 41-47.

Chen, Y., Medioni, G., 1992. Object modelling by registration of multiple range images. *Image and Vision Computing* 10(3), 145-155.

Duffy, B., Quigley, M., Barrell, D. J., Van Dissen, R., Stahl, T., Leprince, S., McInnes, C., Bilderback, E. (2013). Fault kinematics and surface deformation across a releasing bend during the 2010 MW 7.1 Darfield, New Zealand, earthquake revealed by differential LiDAR and cadastral surveying. *Geol. Soc. Am. Bull.*, *125*(3-4), 420-431.

Fialko, Y., 2004. Probing the mechanical properties of seismically active crust with space geodesy: Study of the coseismic deformation due to the 1992 Mw7. 3 Landers (southern California) earthquake. *J. Geophys. Res.* 109, B03307.

Glennie, C. L., Hinojosa-Corona, A., Nissen, E., Kusari, A., Oskin, M. E., Arrowsmith, J. R., & Borsa, A. (2014). Optimization of legacy LiDAR datasets for measuring near-field earthquake displacements. *Geophys. Res. Lett.*, 41 (10), 3494-3501.

Haugerud, R. A., Harding, D. J., Johnson, S. Y., Harless, J. L., Weaver, C. S., Sherrod, B. L., 2003. High-resolution lidar topography of the Puget Lowland, Washington. *GSA Today* 13(6), 4-10.

Kobayashi, T., Tobita, M., Koarai, M., Okatani, T., Suzuki, A., Noguchi, Y., Yamanaka, M., Miyahara, B., 2012. InSAR-derived crustal deformation and fault models of normal faulting earthquake (*M*j 7.0) in the Fukushima-Hamadori area. *Earth Planets Space* 64, 1209-1221.

Lucca, E., Festa, G., Emolo, A., 2012. Kinematic Inversion of Strong-Motion Data Using a Gaussian Parameterization for the Slip: Application to the 2008 Iwate-Miyagi, Japan, Earthquake. *Bull. Seismol. Soc. Am.* 102(6), 2685-2703.

Massonnet, D., Rossi, M., Carmona, C., Adragna, F., Peltzer, G., Feigl, K., Rabaute, T., 1993. The displacement field of the Landers earthquake mapped by radar interferometry. *Nature* 364(6433), 138-142.

Matsu'ura, T., Kase, Y., 2010. Late Quaternary and coseismic crustal deformation across the focal area of the 2008 Iwate-Miyagi Nairiku earthquake. *Tectonophys.* 487, 13-21.

Michel, R., J. P. Avouac, J. P., Taboury, J., 1999. Measuring ground displacements from SAR amplitude images: Application to the Landers earthquake. *Geophys. Res. Lett.* 26(7), 875-878.

Midorikawa, S., Miura, H., 2008. Damage and High-Resolution SAR Image in the 2008 Iwate-Miyagi-Nairiku, Japan Earthquake. *6th International Workshop on Remote Sensing for Disaster Applications.*

Mizoguchi, K., Uehara, S. Ueta, K., 2012. Surface Fault Ruptures and Slip Distributions of the Mw 6.6 11 April 2011 Hamadoori, Fukushima Prefecture, Northeast Japan, Earthquake. *Bull. Seismol. Soc. Am.* 102, 1949-1956.

Mukoyama, S., 2012. Estimation of Ground Deformation Caused by the Earthquake (M7.2) in Japan, 2008, from the Geomorphic Image Analysis of High Resolution LiDAR DEMs. *J. Mountain Sci.* 8, 239-245.

Nakata, T., Imaizumi, T., 2002. Digital Active Fault Map of Japan. *University of Tokyo Press* (in Japanese).

Nissen, E., Krishnan, A. K., Arrowsmith, J. R., Saripalli, S., 2012. Three-dimensional surface displacements and rotations from differencing pre- and post-earthquake LiDAR point clouds. *Geophys. Res. Lett.* 39, L16301.

Nissen, E., Maruyama, T., Arrowsmith, J. R., Elliott, J. R., Krishnan, A. K., Oskin, M. E. & Saripalli, S. (2014). Coseismic fault zone deformation revealed with differential LiDAR: examples from Japanese Mw ~7 intraplate earthquakes. *Earth Planet. Sci. Lett.*, 405, 244-246.

Ohta, Y., Ohzono, M., Miura, S., Iinuma, T., Tachibana, K., Takatsuka, K., Miyao, K., Sato, T., Umino, N., 2008. Coseismic fault model of the 2008 Iwate-Miyagi Nairiku earthquake deduced by a dense GPS network. *Earth Planets Space* 60(12), 1197.

Oskin, M. E., Arrowsmith, J. R., Corona, A. H., Elliott, A. J., Fletcher, J. M., Fielding, E. J., Gold, P. O., Garcia, J. J. G., Hudnut, K. W., Liu-Zeng, J., Teran, O. J., 2012. Near-Field Deformation from the El Mayor-Cucapah Earthquake Revealed by Differential LIDAR. *Science* 335, 702-705.

Ozawa, S., Nishimura, T., Suito, H., Kobayashi, T., Tobita, M., Imakiire, T., 2011. Coseismic and postseismic slip of the 2011 magnitude-9 Tohoku-Oki earthquake. *Nature* 475(7356), 373-376.

Prentice, C. S., Crosby, C. J., Whitehill, C. S., Arrowsmith, J. R., Furlong, K. P., Phillips, D. A., 2009. Illuminating Northern California's Active Faults. *Eos Trans. AGU* 90, 55.

Suzuki, W., Aoi, S., Sekiguchi, H., 2010. Rupture process of the 2008 Iwate–Miyagi Nairiku, Japan, earthquake derived from near-source strong-motion records. *Bull. Seismol. Soc. Am.* 100(1), 256-266.

Takada, Y., Kobayashi, T., Furuya, M., Murakami, M., 2009. Coseismic displacement due to the 2008 Iwate-Miyagi Nairiku earthquake detected by ALOS/PALSAR: preliminary results: *Earth Planets Space* 61, 9-12.

Teza, G., Galgaro, A., Zaltron, N., Genevois, R., 2007. Terrestrial laser scanner to detect landslide displacement fields: A new approach. *Int. J. Rem. Sens.* 28(16), 3425–3446.

Toda, S., Maruyama, T., Yoshimi, M., Kaneda, H., Awata, Y., Yoshioka, T., Ando, R., 2010. Surface rupture associated with the 2008 Iwate-Miyagi Nairiku, Japan, Earthquake and its implications to the rupture process and evaluation of active faults. *Zisin 2 (J. Seismol. Soc. Japan)* 62, 153-178 (in Japanese with English abstract).

Toda, S., Tsutsumi, H., 2013. Spontaneous reactivation of two, subparallel, inland normal faults during the *M*w 6.6 11 April 2011 Iwaki Earthquake triggered by the *M*w 9.0 Tohoku-oki, Japan, Earthquake. *Bull. Seismol. Soc. Am.* 103(2b), 1584-1602.

Yagi, H., Sato, G., Higaki, D., Yamamoto, M., Yamasaki, T., 2009. Distribution and characteristics of landslides induced by the Iwate–Miyagi Nairiku Earthquake in 2008 in Tohoku District, Northeast Japan. *Landslides* 6(4), 335-344.

Yokota, Y., Koketsu, K., Hikima, K., Miyazaki, S. I., 2009. Ability of 1‐Hz GPS data to infer the source process of a medium‐sized earthquake: The case of the 2008 Iwate‐Miyagi Nairiku, Japan, earthquake. *Geophys. Res. Lett.* 36, L12301.